Sombroek, C. S. M., Tiso, P., Renson, L., & Kerschen, G. (2018). Numerical computation of nonlinear normal modes in a modal derivative subspace. *Computers and Structures*, *195*, 34-46. https://doi.org/10.1016/j.compstruc.2017.08.016

Numerical Computation of Nonlinear Normal Modes in a Modal Derivative Subspace

C.S.M. Sombroek[a], P. Tiso[b,*], L. Renson[c], G. Kerschen[d]

[a]*Department of Precision and Microsystems Engineering, Faculty of Mechanical, Maritime and Material Engineering, Delft University of Technology, The Netherlands.*

[b]*Department of Mechanical and Process Engineering, ETH Zürich, Switzerland.*

[c]*Department of Engineering Mathematics, University of Bristol, United Kingdom.*

[d]*Department of Aerospace and Mechanical Engineering, University of Liège, Belgium.*

Abstract

Nonlinear normal modes (NNMs) offer a solid theoretical framework for interpreting a wide class of nonlinear dynamic phenomena. However, the computation of NNMs for large-scale models can be time consuming, particularly when nonlinearities are distributed across the degrees of freedom. In this paper, the NNMs of systems featuring distributed geometric nonlinearities are computed from reduced-order models comprising linear normal modes and modal derivatives. Modal derivatives stem from the differentiation of the eigenvalue problem associated with the underlying linearised vibrations and can therefore account for some of the distortions introduced by nonlinearity. The cases of the Roorda's frame model, a doubly-clamped beam, and a shallow arch discretised with planar beam finite elements are investigated. A comparison between the NNMs computed from the full and reduced-order models highlights the capability of the reduction method to capture the essential nonlinear phenomena, including low-order modal interactions.

Keywords: Nonlinear Normal Modes, Reduced Order Modelling, Modal Derivatives, Geometric Nonlinearities

1. Introduction

The presence of nonlinear phenomena is often neglected in structural dynamics. However, modern engineering designs with stringent constrains on weight lead to flexible structures in which nonlinear geometric effects are significant and can no longer be neglected [1]. Nonlinearity poses important challenges as novel dynamic phenomena that can not be treated with linear analysis can arise. An example is modal interaction where the nonlinear couplings between *linear normal modes* (LNMs) (also often referred to as vibration modes) trigger energy exchanges between modes that can potentially affect the integrity of the structure [2]. From another perspective, nonlinear dynamic phenomena can also be exploited to improve performance as, for instance, in passive micro-mechanical frequency dividers [3] and acoustic switches and rectifiers [4].

Pioneered in the 1960s by Rosenberg [5], the concept of *nonlinear normal modes* (NNMs) has proved useful to address a number of nonlinear phenomena such as mode localization, mode bifurcation and internal resonance. NNMs can be defined as *non-necessarily synchronous periodic oscillations* of the conservative equations of motion of the system in question [6]. In the last decade, a number of numerical methods were developed to compute NNMs (see Ref. [7] for a review). Although some of these methods were successfully applied to real-life structures [8, 2], the computational cost associated with the calculation of NNMs for large-scale models remains an important issue preventing the wider spread of this nonlinear analysis tool in industry. When the structure is linear with localised

*Corresponding author

nonlinearities (as in Refs. [8, 2]), classical linear reduction methods, such as the Craig-Bampton [9] or the Rubin-Mc Neal [10] techniques, can be used to accurately and effectively reduce the dimensionality of the linear system, leading to a significant speed-up of the NNM calculation. However, when the system possesses nonlinearities distributed among all the degrees of freedom (DOFs), as, for instance, when nonlinear geometric effects caused by finite displacements and rotations are present, such linear reduction approaches proved ineffective.

A considerable amount of research effort is directed towards the accurate prediction of the responses of nonlinear geometric systems using *reduced-order models* (ROMs). Generally, ROMs are obtained by detecting a subspace spanned by a reduced-order basis (ROB) on which the solution evolves and then projecting the equation of motion on another basis of the same size. For structural applications characterised by symmetric jacobians, the reduction and projection bases often coincide and the method is termed *Galerkin projection*. Regardless of how the ROB is built, it is crucial to properly account for the nonlinear bending-stretching and torsion-stretching couplings triggered by the finite deflections and rotations. Reduction methods differ in the way these couplings are accounted for in the ROB. In a recent approach, termed *implicit condensation and expansion* (ICE) [11], membrane displacements are recovered from a basis of nonlinear static solutions. The computation of NNMs using this ICE method was investigated in Ref. [12]. An alternative approach to account for the membrane displacements is the concept of *modal derivatives* (MDs). Previous contributions [13, 14, 15, 16, 17, 18] have shown using transient analysis that the essential distortions introduced by nonlinearity can be captured by combining LNMs and MDs in a single ROB. As it will be made clear in this paper, one of the merits of this approach lies in the systematic way MDs are derived, once the relevant LNMs have been selected for the linearised dynamics.

The transient analysis of complex nonlinear systems using, e.g., Newmark's time stepping method, is well-established. However, in addition to their substantial computational cost, time series do not bring much detailed information about the dynamics of a nonlinear system. In this context, it is therefore valuable to calculate features, such as nonlinear frequency response curves and NNMs, which give more physical insight. For instance, it can be shown that resonant vibrations, which are key to the practitioner, occur in the vicinity of nonlinear normal modes. NNMs are also able to capture modal interactions. So calculating NNMs and related frequencies is not just an intellectual exercise per se, but it is of great engineering relevance. In this paper, the computation of NNMs of planar, geometrically nonlinear structures discretised using the finite element (FE) method is investigated. The FE models are reduced via Galerkin projection, using a ROB composed of LNMs and MDs. The accuracy of the reduction in capturing the NNMs, including modal interactions, is discussed. The paper is organised as follows. Section 2 introduces the governing equations of motion and presents the underlying theory of Galerkin projection techniques. The concept of MDs is also reviewed. The method used for computing NNMs is briefly summarised in Section 3. In Section 4, three numerical examples of geometric nonlinear models are presented: the Roorda's frame model (Section 4.1), a doubly-clamped beam (Section 4.2), and a shallow arch (Section 4.3). The NNMs obtained for the full and reduced models are compared in order to demonstrate the effectiveness of the proposed approach.

2. Governing Equations and Model Reduction using Galerkin Projection

The equations of motion of a generic free vibrating, undamped system discretised using the FE method can be written as

$$\begin{cases} \mathbf{M}\ddot{\mathbf{y}}(t) + \mathbf{K}\mathbf{y}(t) + \mathbf{f}^{nl}(\mathbf{y}(t)) = \mathbf{0}, \\ \mathbf{y}(0) = \mathbf{y}_0, \\ \dot{\mathbf{y}}(0) = \dot{\mathbf{y}}_0, \end{cases} \tag{1}$$

where $\mathbf{y}(t) \in \mathbb{R}^n$ is the generalised displacement vector, $\mathbf{M} \in \mathbb{R}^{n\times n}$ and $\mathbf{K} \in \mathbb{R}^{n\times n}$ are the linear mass and stiffness matrices, respectively; $\mathbf{f}^{nl}(\mathbf{y}(t)) : \mathbb{R}^n \mapsto \mathbb{R}^n$ is the nonlinear force vector. The initial conditions for the displacement and velocity vectors are denoted by $\mathbf{y}_0$ and $\dot{\mathbf{y}}_0$, respectively.

In Eq. (1), internal forces are explicitly separated in a linear and nonlinear part. In this work, the nonlinear forces $\mathbf{f}^{nl}$ emanate from geometric nonlinearities, modelled with the von-Karman kinematic assumptions that relate axial strains to the square of rotations [19]. This model yields discretised forces that are up to cubic order in $\mathbf{y}$. The von-Karman kinematic model is adequate for a large class of problems featuring elastic deflections of the order of the thickness. The numerical examples considered in this study focus on planar structures modelled with beam

elements. However, the presented treatment is general and able to handle tridimensional problems, such as shells and continuum solids. From this point on, the time dependency is omitted for clarity.

In practical applications, the size n of Eq. (1) is usually large. The number of unknowns can be reduced to k, with $k \ll n$, by projecting the generalised displacement vector $\mathbf{y}$ on a suitable time-independent ROB $\mathbf{\Psi} \in \mathbb{R}^{n \times k}$ as:

$$\mathbf{y} \approx \mathbf{\Psi}\mathbf{q}, \tag{2}$$

where $\mathbf{q}(t) \in \mathbb{R}^k$ is the vector of reduced displacements. The governing equations can then be projected on the chosen basis $\mathbf{\Psi}$ in order to make the equilibrium residual orthogonal to the subspace in which the solution $\mathbf{q}$ is sought. This results in a reduced system of k nonlinear equations:

$$\mathbf{\Psi}^T\mathbf{M}\mathbf{\Psi}\ddot{\mathbf{q}} + \mathbf{\Psi}^T\mathbf{K}\mathbf{\Psi}\mathbf{q} + \mathbf{\Psi}^T\mathbf{f}^{nl}(\mathbf{\Psi}\mathbf{q}) = \mathbf{0}, \tag{3}$$

or, equivalently,

$$\hat{\mathbf{M}}\ddot{\mathbf{q}} + \hat{\mathbf{K}}\mathbf{q} + \hat{\mathbf{f}}^{nl}(\mathbf{\Psi}\mathbf{q}) = \mathbf{0}. \tag{4}$$

The reduced mass matrix $\hat{\mathbf{M}}$ and stiffness matrix $\hat{\mathbf{K}}$ do not depend on $\mathbf{q}$ and can be calculated offline. We refer to the numerical solution $\mathbf{y}$ of Eq. (1) as the *full* solution, while $\mathbf{u} = \mathbf{\Psi}\tilde{\mathbf{q}}$ is called *reduced* solution, $\tilde{\mathbf{q}}$ being the solution of Eq. (4). The key of a good reduction method is to find a suitable ROB $\mathbf{\Psi}$ that is able to accurately reproduce the full solution.

2.1. Reduction Basis for Geometrically Nonlinear Systems

The projection of the equations of motion on a basis formed with a reduced set of LNMs is a well-known approach in linear structural dynamics. Its main advantage is that the resulting ROM consists of a set of uncoupled equations that can be solved separately. For nonlinear systems, such an approach is limited because LNMs do not decouple the equations of motion and are able, by definition, to reproduce the motion only in a small neighbourhood of the equilibrium. Therefore LNMs do not constitute an effective reduction basis when the dynamics features large displacements. Some pioneering works proposed to update the ROB by computing vibration modes around arbitrary dynamic configurations attained by the system as the time integration proceeds [20, 21, 22]. However, such linear modes extracted about an arbitrary, non-equilibrium configuration do not represent the local dynamics of the motion; therefore it is not surprising that these approaches suffered from basis updates that were frequent enough to compromise the effectiveness of the method.

The ideal situation is to have a constant ROB which is able to account for the nonlinear behaviour. In that respect, MDs proved to be an effective addition to a ROB basis of LNMs, allowing the accurate transient analysis of geometrically nonlinear structures [23]. MDs stem from the directional derivatives of the linear eigenvalue problem in the direction of the LNMs. The derivation and computation of MDs are briefly reviewed for completeness.

We start by assuming a nonlinear mapping $\mathbf{\Gamma}$ between the full solution $\mathbf{y} \in \mathbb{R}^n$ and a vector of reduced linear modal coordinates $\mathbf{q} \in \mathbb{R}^k$,

$$\mathbf{y} - \mathbf{y}_{eq} = \mathbf{\Gamma}(\mathbf{q}), \tag{5}$$

where $\mathbf{y}_{eq}$ is the equilibrium configuration, and $k \ll n$. A Taylor series expansion of Eq. (5) leads to

$$\mathbf{y} - \mathbf{y}_{eq} = \frac{\partial \mathbf{\Gamma}}{\partial q_i}\Big|_{eq} q_i + \frac{1}{2}\frac{\partial^2 \mathbf{\Gamma}}{\partial q_i \partial q_j}\Big|_{eq} q_i q_j + \dots, \tag{6}$$

where Einstein's summation convention for repeated indeces is used. The first-order derivative in Eq. (6) can be written as

$$\frac{\partial \mathbf{\Gamma}}{\partial q_i}\Big|_{eq} = \boldsymbol{\phi}_i \tag{7}$$

where $\boldsymbol{\phi}_i$ is an eigenvector of the problem

$$\left(\mathbf{K} - \omega_i^2\mathbf{M}\right)\boldsymbol{\phi}_i = \mathbf{0}, \tag{8}$$

obtained by linearising the equations of motion at the equilibrium $\mathbf{y}_{eq}$. Eigenvectors $\boldsymbol{\phi}_i$ correspond to the LNMs of the system and are assumed to be normalised such that the orthogonality conditions

$$\boldsymbol{\phi}_i^T \mathbf{M} \boldsymbol{\phi}_j = \delta_{ij}, \tag{9}$$

$$\boldsymbol{\phi}_i^T \mathbf{K} \boldsymbol{\phi}_j = \omega_i^2 \delta_{ij}, \tag{10}$$

where δ_{ij} is the Kronecker's delta function, hold.

Following Eq. (7), the second-order derivative term of Eq. (6) becomes

$$\frac{\partial^2 \boldsymbol{\Gamma}}{\partial q_i \partial q_j}\Big|_{eq} = \frac{\partial \boldsymbol{\phi}_i}{\partial q_j}\Big|_{eq} \tag{11}$$

and represents the directional derivative of the LNMs at the equilibrium. In other words, this term represents how LNM $\boldsymbol{\phi}_i$ changes when a displacement affine to LNM $\boldsymbol{\phi}_j$ is imposed. These terms can be conveniently calculated by differentiation of the eigenvalue problem (8) with respect to the modal coordinates, as

$$\left(\mathbf{K} - \omega_i^2 \mathbf{M}\right) \frac{\partial \boldsymbol{\phi}_i}{\partial q_j} + \left(\frac{\partial \mathbf{K}^{nl}}{\partial q_j}\Big|_{eq} - \frac{\partial \omega_i^2}{\partial q_j} \mathbf{M} \right) \boldsymbol{\phi}_i = \mathbf{0}, \tag{12}$$

where the tangent stiffness matrix is $\mathbf{K}^{nl} = \partial \mathbf{f}^{nl} / \partial \mathbf{y}$ and $\partial \mathbf{K} / \partial \mathbf{y}$ equals zero. Eq. (12) can be rearranged to get

$$\left(\mathbf{K} - \omega_i^2 \mathbf{M}\right) \boldsymbol{\theta}_{ij} = -\frac{\partial \mathbf{K}^{nl}}{\partial q_j}\Big|_{eq} \boldsymbol{\phi}_i + \frac{\partial \omega_i^2}{\partial q_j}\Big|_{eq} \mathbf{M} \boldsymbol{\phi}_i, \tag{13}$$

where $\boldsymbol{\theta}_{ij} = \frac{\partial \boldsymbol{\phi}_i}{\partial q_j}$ is called the modal derivative of mode i with respect to mode j. The solution of the linear problem (13) for $\boldsymbol{\theta}_{ij}$ is not straightforward, since the term on the left hand side is singular. There are different methods available in the literature to tackle this problem, for instance Nelson's method [24], or pseudo inverse approaches as discussed in [25]. Here we employ a direct method to obtain a unique solution. The set of equations (13) is augmented with the derivative of the mass normalization condition with respect to the modal coordinates:

$$\boldsymbol{\phi}_i^T \mathbf{M} \boldsymbol{\theta}_{ij} = \mathbf{0}, \qquad \forall i, j = 1, \dots, k, \tag{14}$$

to finally obtain

$$\begin{bmatrix} \mathbf{K} - \omega_i^2 \mathbf{M} & -\mathbf{M}\boldsymbol{\phi}_i \\ -\left(\mathbf{M}\boldsymbol{\phi}_i\right)^T & 0 \end{bmatrix} \begin{bmatrix} \boldsymbol{\theta}_{ij} \\ \frac{\partial \omega_i^2}{\partial q_j}\Big|_{eq} \end{bmatrix} = \begin{bmatrix} -\frac{\partial \mathbf{K}^{nl}}{\partial q_j}\Big|_{eq} \boldsymbol{\phi}_i \\ 0 \end{bmatrix}, \tag{15}$$

which can eventually be solved to obtain the modal derivative $\boldsymbol{\theta}_{ij}$.

Previous contributions have shown that an effective ROB for geometrically nonlinear problems can be formed by combining the dominant LNMs with their corresponding MDs as [13, 14, 16]:

$$\boldsymbol{\Psi} = [\boldsymbol{\phi}_1, \dots, \boldsymbol{\phi}_k, \dots, \boldsymbol{\theta}_{ij}, \dots], \qquad \forall i, j = 1, \dots, k. \tag{16}$$

Indeed, such a ROB naturally and systematically includes the dominant displacement modes that are necessary to account for geometric nonlinear effects, such as bending-stretching and torsion-stretching couplings. Their calculation requires moderate computational cost compared to the effort required to extract LNMs.

3. Computation of Nonlinear Normal Modes

For conservative systems, NNMs are sought as periodic solutions of the nonlinear equations of motion. A NNM is traced in a so-called Frequency-Energy Plot (FEP): each point of this diagram represents a periodic solution at a specific level of energy. As discussed, the tracking of a NNM for increasing energy levels is prohibitive for

the full system (1). Instead, the NNM is sought for the low-size ROM (3). A two-step algorithm combining the shooting method and pseudo-arclength continuation is used, as extensively discussed in [26]. This approach is briefly summarised in this section for sake of completeness. First, the ROM (3) is written in a state-space form as

$$\dot{\mathbf{z}} = \begin{bmatrix} \dot{\mathbf{q}} \\ -\hat{\mathbf{M}}^{-1}\left(\hat{\mathbf{K}}\mathbf{q} + \hat{\mathbf{f}}^{nl}(\boldsymbol{\Psi}\mathbf{q})\right) \end{bmatrix} = \mathbf{g}(\mathbf{z}), \tag{17}$$

where $\mathbf{z}$ is the state vector of the system $\mathbf{z}^T = [\mathbf{q}^T \dot{\mathbf{q}}^T]$. Note that, in the system (17), the reduction basis $\boldsymbol{\Psi}$ is established once for all prior the tracking of the NNM for increasing energy levels. We use the shooting method to obtain periodic solutions of Eq. (17). The shooting method is a well-established numerical technique for solving two-point boundary-value problems and can be applied to the periodicity condition

$$\mathbf{H}(T, \mathbf{z}_{p_0}) = \mathbf{z}_p(T, \mathbf{z}_{p_0}) - \mathbf{z}_{p_0} = \mathbf{0}, \tag{18}$$

which expresses the difference between the state of the system $\mathbf{z}_p(T, \mathbf{z}_{p_0})$ at time T and the initial state $\mathbf{z}_{p_0}$. A solution $\mathbf{z}_p(t, \mathbf{z}_{p_0})$ is periodic if $\mathbf{z}_p(t, \mathbf{z}_{p_0}) = \mathbf{z}_p(t+T, \mathbf{z}_{p_0})$ where T is the minimal period. In a shooting algorithm, the period T and the initial conditions $\mathbf{z}_{p_0}$ that lead to a periodic motion are found iteratively. More specifically, numerical direct time integration is carried out using an initial guess of the periodic solution and Eq. (18) is evaluated. The initial guess is iteratively corrected by means of a Newton-Raphson procedure to converge to the actual solution. In this work, time integration is performed using a standard, implicit Newmark scheme.

An important remark in the resolution of the boundary-value problem formulated in Eq. (18) is that the phase of the periodic solutions is not unique. If $\mathbf{z}_p(t)$ is solution of the equations of motion, then $\mathbf{z}_p(t+\Delta t)$ is geometrically the same solution in state space for any Δt. Hence, an additional condition $h(\mathbf{z}_{p_0}) = 0$, termed phase condition, is specified to remove the arbitrariness of the initial conditions. Following the approach proposed in [26], the modal velocities are set equal to zero. In summary, an isolated NNM motion is computed by solving the augmented two-point boundary-value problem defined by the two relations

$$\mathbf{H}(T, \mathbf{z}_{p_0}) = \mathbf{0}, \tag{19}$$

$$h(\mathbf{z}_{p_0}) = 0. \tag{20}$$

Say that a certain solution $\mathbf{z}^k_{p_0}, T^k$, not satisfying Eq. (18), is found. One then wishes to correct it by requiring

$$\mathbf{H}(T^k + \Delta T^k, \mathbf{z}^k_{p_0} + \Delta \mathbf{z}^k_{p_0}) = \mathbf{0}. \tag{21}$$

A Taylor series expansion of (21) then writes

$$\mathbf{H}(T^k, \mathbf{z}^k_{p_0}) + \left.\frac{\partial \mathbf{H}}{\partial \mathbf{z}_{p_0}}\right|_{\mathbf{z}^k_{p_0}, T_k} \Delta \mathbf{z}^k_{p_0} + \left.\frac{\partial \mathbf{H}}{\partial T}\right|_{\mathbf{z}^k_{p_0}, T_k} \Delta T^k + \cdots = \mathbf{0}. \tag{22}$$

By neglecting terms of second order and higher, and rearranging in matrix form, one can write a linear system of equations

$$\begin{bmatrix} \left.\frac{\partial \mathbf{H}}{\partial \mathbf{z}_{p_0}}\right|_{\mathbf{z}^k_{p_0}, T_k} & \left.\frac{\partial \mathbf{H}}{\partial T}\right|_{\mathbf{z}^k_{p_0}, T_k} \\ \left.\frac{\partial h^T}{\partial \mathbf{z}_{p_0}}\right|_{\mathbf{z}^k_{p_0}} & 0 \end{bmatrix} \begin{bmatrix} \Delta \mathbf{z}^k_{p_0} \\ \Delta T^k \end{bmatrix} = \begin{bmatrix} -\mathbf{H}(\mathbf{z}^k_{p_0}, T^k) \\ -h(\mathbf{z}^k_{p_0}) \end{bmatrix}, \tag{23}$$

where the second row stems from the differentiation of the phase constraint. The system (23) can be solved to find the corrections $\Delta \mathbf{z}^k_{p_0}$ and ΔT^k. The first block of the coefficient matrix $\frac{\partial \mathbf{H}}{\partial \mathbf{z}_{p_0}}$ is actually found by differentiating the equation of motion (17) as

$$\frac{\partial}{\partial \mathbf{z}_0}\left[\dot{\mathbf{z}}(t, \mathbf{z}_0\right] = \frac{\partial}{\partial \mathbf{z}_0}\left[\mathbf{g}(\mathbf{z}(t, \mathbf{z}_0))\right], \tag{24}$$

which can be rewritten as

$$\frac{d}{dt}\left[\frac{\partial \mathbf{z}(t, \mathbf{z}_0)}{\partial \mathbf{z}_0}\right] = \left.\frac{\partial \mathbf{g}(\mathbf{z})}{\partial \mathbf{z}}\right|_{\mathbf{z}(t, \mathbf{z}_0)} \frac{\partial \mathbf{z}(t, \mathbf{z}_0)}{\partial \mathbf{z}_0}. \tag{25}$$

The last equation (25) is linear - and therefore cheap - within one time step of the numerical time integration, as the gradient $\frac{\partial \mathbf{g}(\mathbf{z})}{\partial \mathbf{z}}\Big|_{\mathbf{z}(t,\mathbf{z}_0)}$ is available from the solution of the state.

To trace out the family of periodic solutions that describe the considered NNM, shooting is combined with a pseudo-arc-length continuation technique. Starting from a known periodic solution $[\mathbf{z}_{p_0,(j)}, T_{(j)}]$, continuation proceeds in two steps, namely a prediction and a correction. In the prediction step, the next NNM motion $[\mathbf{z}^{*T}_{p_0,(j+1)}, T^*_{(j+1)}]^T$ is predicted tangentially to the NNM branch, as

$$\begin{bmatrix} \mathbf{z}^*_{p_0,(j+1)} \\ T^*_{(}j+1) \end{bmatrix} = \begin{bmatrix} \mathbf{z}_{p_0,(j)} \\ T_{(}j) \end{bmatrix} + s(j) \begin{bmatrix} \mathbf{p}_{z,(j)} \\ p_{T,(j)} \end{bmatrix}, \tag{26}$$

where $s(j)$ is a user-specified length, and the search direction is the kernel of the Hessian matrix in (25) at the last converged solution

$$\begin{bmatrix} \frac{\partial \mathbf{H}}{\partial \mathbf{z}_{p_0}}\Big|_{\mathbf{z}_{p_0,(j)},T_{(j)}} & \frac{\partial \mathbf{H}}{\partial T}\Big|_{\mathbf{z}_{p_0,(j)},T_{(j)}} \\ \frac{\partial h^T}{\partial \mathbf{z}_{p_0}}\Big|_{\mathbf{z}_{p_0,(j)}} & 0 \end{bmatrix} \begin{bmatrix} \mathbf{p}_{\mathbf{z},(j)} \\ p_{T,(j)} \end{bmatrix} = \begin{bmatrix} \mathbf{0} \\ 0 \end{bmatrix}. \tag{27}$$

Subsequently, this prediction is corrected using shooting and by constraining the corrections of the period and initial conditions to be orthogonal to the prediction direction as

$$[\mathbf{p}_{\mathbf{z},(j)} \;\; p_{T,(j)}]^T [\Delta \mathbf{z}^k_{p_0,(j+1)} \;\; \Delta T^k_{(j+1)}] = 0. \tag{28}$$

4. Numerical Examples

4.1. Example 1: Roorda's frame

The first example consists of the so-called Roorda's frame sketched in Figure 1(a) [27]. This structure is made of two identical beams that have rectangular cross sections. The beams are rigidly-connected together at one end to form a right angle and hinged at the other end. Each beam is discretised using 25 elements, leading to 149 DOFs for the whole structure. The geometric and material properties of the beams are reported in Table 1.

The natural frequency of the first LNM of the structure is 739 rad/s and its modal shape is shown in Figure 1(b). This first mode corresponds to the first bending mode of the two beams. Both beams can be considered to oscillate in phase as the vertical and horizontal beams exhibit simultaneously negative (or positive) displacements along the x and y axes, respectively. The mode is also characterised by zero displacement at the connection between the two beams. When the amplitude of the first mode increases, geometric nonlinearities couple bending and stretching motions, which, intuitively, results in forces that pull the corner of the frame towards its centre. This effect is captured by the MD of first LNM with respect to itself, i.e. θ_{11}, as illustrated in Figure 1(c).

The first NNM of the Roorda's frame is presented in Figure 2. For low energies, the frequency of the NNM is close to the first natural frequency and remains almost constant. For higher energies or, equivalently, for larger oscillation amplitudes, the NNM frequency increases as a consequence of the hardening effect introduced by the geometric nonlinearities. The time series of x_{13} (−) located on the vertical beam and y_{39} (−−) located on the horizontal beam are inset in Figure 2 for three periodic solutions along the NNM. Both coordinates have the same relative position along the beams and have therefore identical time series in the linear case. This symmetry property appears to be preserved in the nonlinear case although small differences are observed at high energy. However, at such high energy levels, displacements exceed beam thicknesses and the von-Karman kinematic assumptions underlying the

Young's modulus [GPa]	**Density** [kg/m^3]	**Length** [m]	**Width** [m]	**Thick.** [m]
210	7800	0.1	1×10^{-3}	5×10^{-4}

Table 1: Material and geometric properties of the beams used in the Roorda's frame.

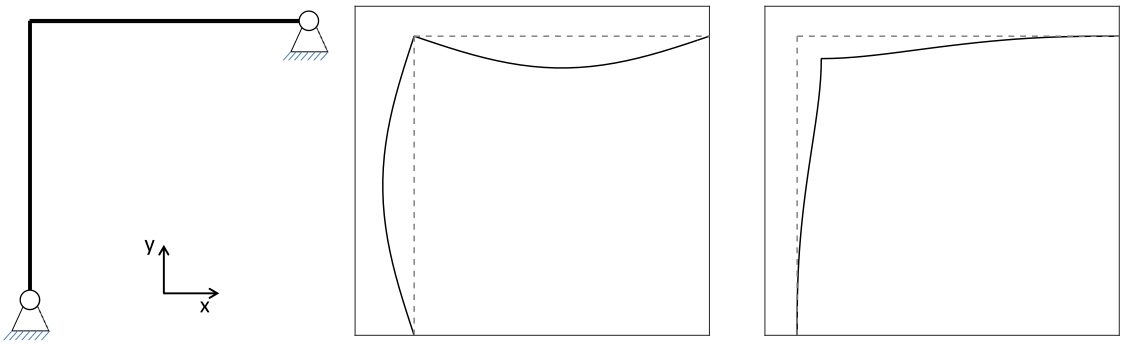

Figure 1: Roorda's frame model. (a) Structure schematics; (b) Structure deformed according to first LNM (▬); (c) Structure deformed according to the modal derivative θ_{11} (▬). Undeformed structure in grey (▬ ▬).

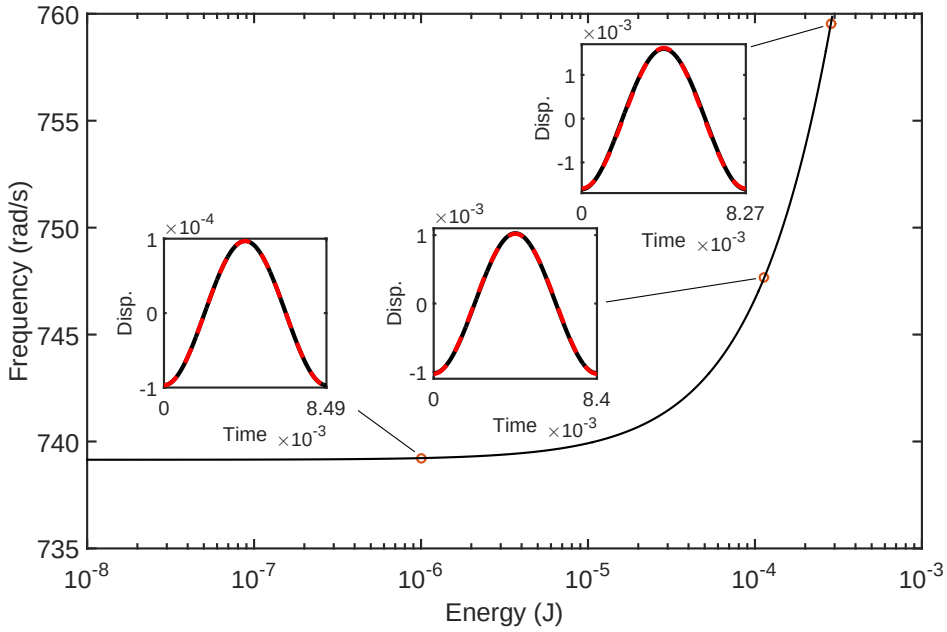

Figure 2: First NNM of the Roorda's frame model. The time series of 3 periodic solutions are inset along the NNM. The time axis has been restricted to $0 - T/2$, where T is the minimal motion period. Displayed coordinates are x_{13} (▬) and y_{39} (▬).

FE model are no longer valid. Throughout, time series show a rather simple frequency content and no sign of distortions due to the presence of potential higher harmonics in the response.

Three different ROMs were considered for computing the first NNM of Roorda's structure, as shown in Figure 3. The first ROB, Ψ_1 (–), contains the first 30 LNMs and clearly fails to capture the NNM computed for the full model (– in Figure 3). This seemingly simple system has a more complex dynamics than the FEP and time series in Figure 2 might suggest, including couplings between the LNMs. These couplings can be observed by projecting the periodic solutions corresponding to the first NNM on the basis of LNMs (not represented for conciseness). As such, the system requires a rather rich linear basis to reach an accurate representation. The second ROB, Ψ_2,

is composed of the first LNM and its own MD and yields significantly better results. This clearly shows the role of MDs in capturing the essential spatial deformations induced by the nonlinearities. Finally, to reproduce the full model response without any visible difference a third ROB, Ψ_3, that includes the first five LNMs and their respective MDs for a total of 20 DOFs was required.

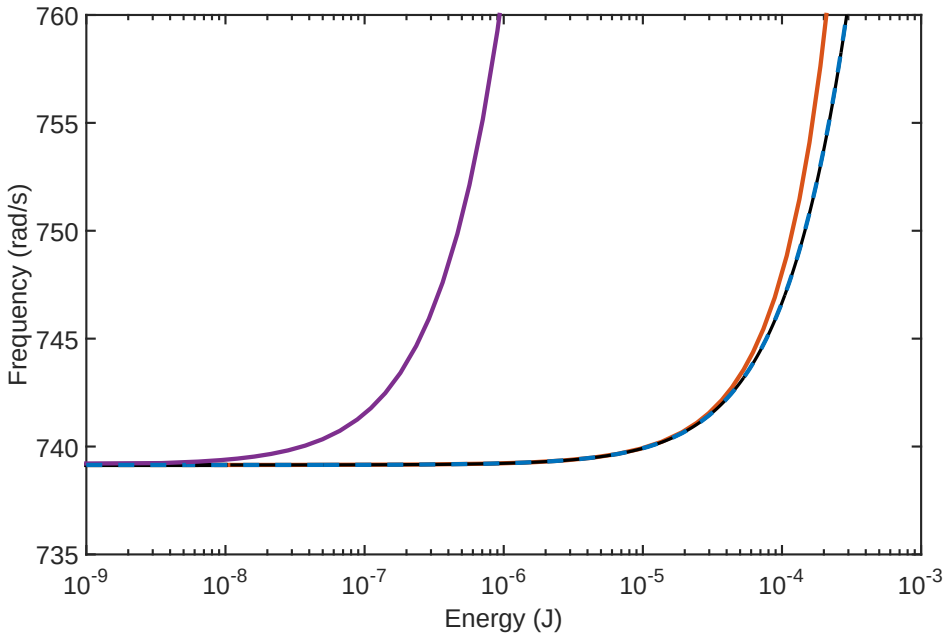

Figure 3: First NNM of the Roorda's frame model. Comparison between the FEP obtained for the full model (▬) and for ROMs that include: $[\boldsymbol{\phi}_1 - \boldsymbol{\phi}_{30}]$ (▬), $[\boldsymbol{\phi}_1\ \boldsymbol{\theta}_{11}]$ (▬), and $[\boldsymbol{\phi}_1\ ...\ \boldsymbol{\phi}_5\ \boldsymbol{\theta}_{11}\ \boldsymbol{\theta}_{12}\ ...\ \boldsymbol{\theta}_{55}]$ (▬ ▬).

One could argue that the mode shapes necessary to represent the bending-stretching coupling introduced by nonlinearity could be extracted from higher-frequency LNMs. This statement is generally correct but high-frequency modes of large-scale systems are typically not computed. Furthermore, even if they were computed, finding which modes are important would remain challenging and a wide selection of them might be necessary to capture the nonlinear behaviour correctly. In this example, the LNM that ressembles the most $\boldsymbol{\theta}_{11}$ according to the modal assurance criterion (MAC) was identified as LNM 122, reaching a MAC value of approximately 72 %. This LNM possesses a very high natural frequency, i.e. $2.3\times 10^6\ rad/s$, which made the computation of the NNM impractical when it was included in the ROB.

4.2. Example 2: A Straight Clamped-Clamped Beam

The second example is the straight, clamped-clamped beam illustrated in Figure 4. The beam is discretised using 30 elements, leading to a full model with 87 DOFs. The geometrical and material properties of the beam are listed in Table 2. The first three LNMs of such a planar structure corresponds to bending modes as is well-known in the literature. Their natural frequencies are 334 rad/s, 921 rad/s, and 1805 rad/s, respectively; their mode shapes are depicted in Figure 5.

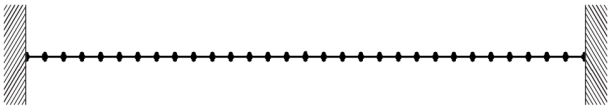

Figure 4: Straight, clamped-clamped beam structure.

Young's modulus [GPa]	Density [kg/m^3]	Length [m]	Area [m^2]	I [m^4]
210	8750	1	1×10^{-4}	8.33×10^{-10}

Table 2: Dimensions and material properties of the clamped-clamped beam structure.

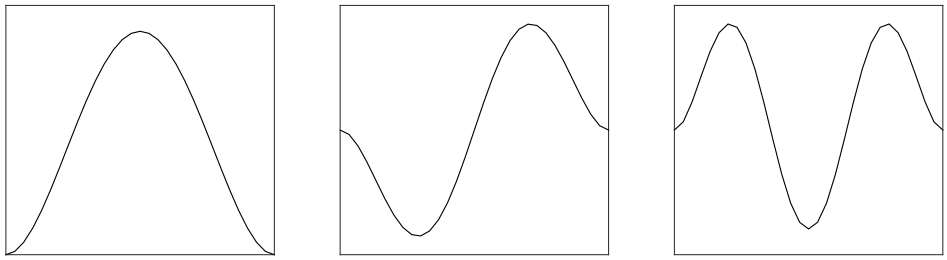

(a) (b) (c)

Figure 5: First three LNMs of the clamped-clamped beam structure presented in Figure 4.

The MDs corresponding to the first three LNMs are given in Figure 6. Similarly to Example 1, it is possible to interpret MDs physically. For instance, the MD of the first LNM with respect to the second one, θ_{12}, exhibits its maximum in-plane (i.e. horizontal) displacements where LNM2 reaches its maxima. The in-plane stretching is however reduced at the centre of the beam where the second LNM has a vibration node. More generally, as a result of the bending nature of the LNMs, all the MDs exhibit in-plane displacements only. Figure 6 further shows the symmetric nature of MDs, i.e. $\theta_{ij} = \theta_{ji}$. Although such physical interpretations become challenging for higher-frequency modes, this clearly shows that MDs capture the underlying physics of geometric nonlinearities and bending-stretching couplings.

4.2.1. First NNM

The FEP of the first NNM (denoted NNM1) is represented in Figure 7. For low energies, the oscillation frequency is constant in function of the energy and the system exhibits a linear-like behaviour. For energies larger than 10^{-2} J, the effects of nonlinearities become apparent, causing an increase in frequency. At about 370 rad/s, the FEP shows the presence of a thin loop, termed internal resonance tongue, indicating an energy exchange between different modes of the structure. This interaction occurs between NNM1 and NNM3 which, around 370 rad/s, have their oscillation frequencies in a 5:1 ratio. A close-up of the interaction region is provided in Figure 7. Along the resonance tongue, the motion gradually evolves from NNM1 to NNM3, and then back to NNM1. This transition is illustrated using the time series of four specific points close to and on the interaction tongue (Figures 7(a-d)). The displayed time series correspond to the vertical displacement of the middle of the beam. As the tip of the resonance tongue is approached (Figure 7(a) to 7(b)), the presence of the fifth harmonic in the response increases. At the tip of the tongue, the fifth harmonic is (almost) exclusively present and the motion of the structure is very similar to NNM3. After the tip of the tongue, a similar but reversed transition occurs and a motion similar to NNM1 is finally recovered (Figure 7(d)). Note that the ratio between the linear natural frequencies, ω_3/ω_1, is 5.4 which indicates that it is not required to have an integer ratio between the natural frequencies for an internal resonance to occur. This is caused by different energy dependency of the modes involved; here the frequency of NNM1 increases faster than the frequency of NNM3.

The reproduction of NNM1 FEP using different ROMs is now investigated with a particular emphasis on the contribution of the different MDs to the accuracy of the solution. Figure 8(a) compares the FEP obtained with a first ROB, $\mathbf{\Psi}_1$, that includes the first LNM ($\mathbf{\Psi}_1 = [\boldsymbol{\phi}_1]$) and a second ROB, $\mathbf{\Psi}_2$, that includes the first LNM and its own modal derivative ($\mathbf{\Psi}_2 = [\boldsymbol{\phi}_1\ \boldsymbol{\theta}_{11}]$). The second basis, which comprises 2 DOFs, reproduces the overall NNM better than $\mathbf{\Psi}_1$. However, both ROMs do not capture the interaction tongue. To capture it, the interacting LNM, $\boldsymbol{\phi}_3$, has to be included in the ROB. Figure 8(b) shows the result obtained with a third ROB, $\mathbf{\Psi}_3$, that includes $\boldsymbol{\phi}_1$, $\boldsymbol{\phi}_3$, and $\boldsymbol{\theta}_{11}$. The overall shape of the NNM is further improved and a 5:1 interaction tongue has appeared. However, the comparison with the reference results obtained with the full model (−) shows that the whole shape of the tongue,

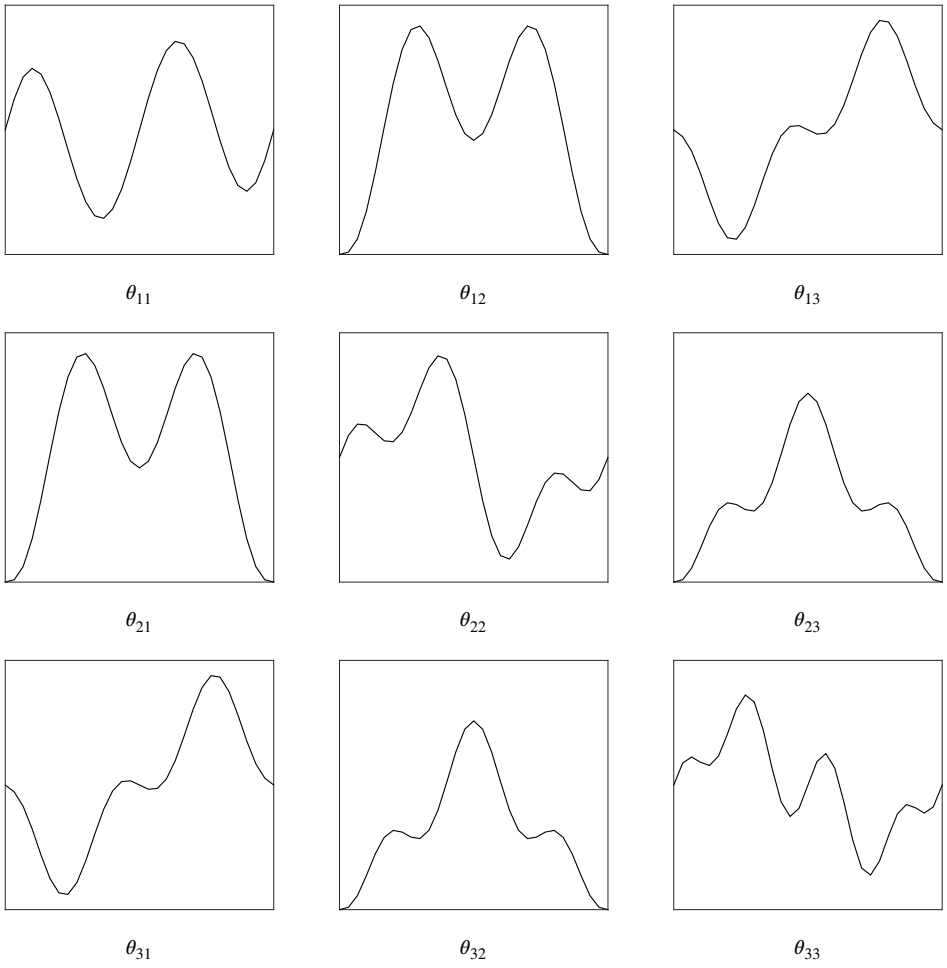

Figure 6: MDs of the first three LNMs with respect to each other for the clamped-clamped beam system. MDs exhibit in-plane displacements only (▬) (plotted on the y-axis for clarity). Out-of-plane displacements (not represented) are all equal to zero.

including start and end regions, is not correctly captured. To accurately account for the couplings between modes 1 and 3, $\boldsymbol{\theta}_{13}$ has to be added, leading to a fourth ROB, $\boldsymbol{\Psi}_4 = [\boldsymbol{\phi}_1\ \boldsymbol{\phi}_3\ \boldsymbol{\theta}_{11}\ \boldsymbol{\theta}_{13}]$. For this ROM, the overall shape of the interaction tongue is well captured and the remaining discrepancies are restricted to high energies and the tip of the tongue (Figure 8(c)). To capture NNM1 with no visible difference with the full-order system, MD $\boldsymbol{\theta}_{33}$ has to be included in the model (see (−−) in Figure 8(d)). Similarly to $\boldsymbol{\theta}_{11}$ which improves the overall shape of NNM1, $\boldsymbol{\theta}_{33}$ improves the accuracy with which the overall shape of NNM3 can be calculated and therefore influences strongly the end of the interaction tongue where the motion is dominated by NNM3. In summary, the full NNM1 branch, including the modal interaction, is accurately captured using a ROM containing five DOFs, and each LNM and MD in the basis has its own specific contribution in representing the response of the full system. For comparison, Figure 8 also shows the FEP obtained with a ROM, $\boldsymbol{\Psi}_6$, containing the first five LNMs, without MDs (− • −). Similarly to the Roorda's frame example, LNMs are clearly ineffective to capture the nonlinear distortions and both the overall shape of the NNM and the modal interaction tongue are not accurately represented.

4.2.2. Second NNM

The FEP corresponding to NNM2 is presented in a solid black line in Figure 9. It shows the presence of two interaction tongues corresponding to 1) a 3:1 interaction with NNM4, starting at approximately 1000 rad/s, and 2) a 5:1 interaction with NNM6, starting at approximately 1300 rad/s. Here again, the natural frequencies are not commensurate and $\omega_4/\omega_2 = 3.2$ and $\omega_6/\omega_2 = 6.8$, respectively. Between 1350 and 1400 rad/s, two additional resonance tongues branch off the interaction tongue with NNM6. These secondary interactions involve NNM15

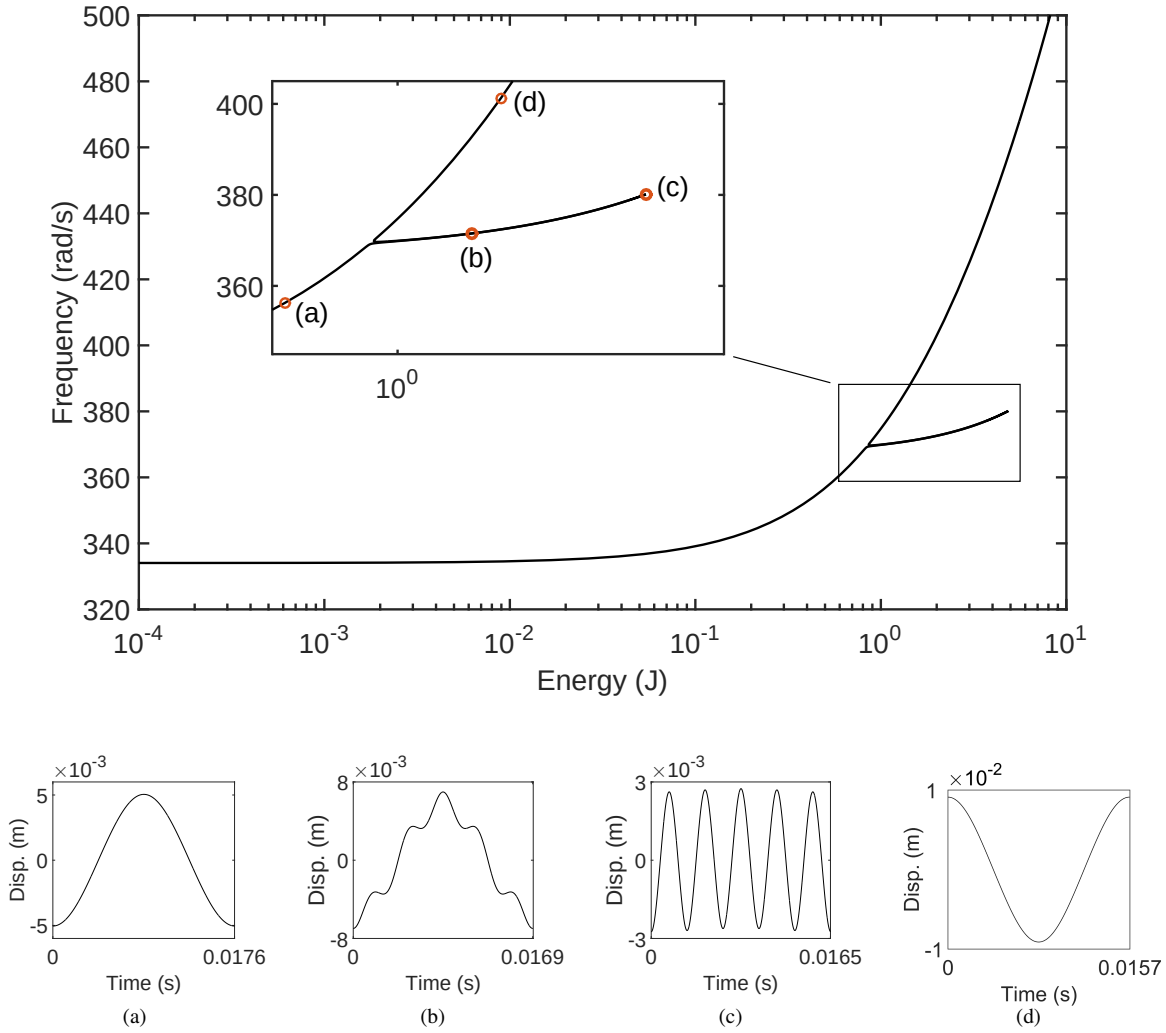

Figure 7: FEP of the first NNM of the clamped-clamped beam structure computed for the full FE model. A close-up of the 5:1 interaction with NNM3 is inset. (a-d) Vertical displacement at the middle of the beam for the periodic solutions reported in the FEP.

and NNM16 through high-order harmonics: the 23rd and 24th, respectively. Tracing out these solution branches revealed to be time consuming as the continuation algorithm required very small continuation steps and showed poor convergence. As such, both secondary branches presented in Figure 9 are incomplete.

To accurately capture internal resonances, the previous section illustrated the necessity to include in the ROB the interacting LNMs as well as their corresponding MDs. Similar results are observed here. Figure 9 compares the second NNM obtained for the full model and for three different ROMs. The first ROM, $\mathbf{\Psi}_1^2$ includes $[\boldsymbol{\phi}_2\ \boldsymbol{\phi}_4\ \boldsymbol{\theta}_{22}\ \boldsymbol{\theta}_{24}\ \boldsymbol{\theta}_{44}]$ and captures well the overall NNM and the first interaction with NNM4 (Figure 9(a)). The second interaction with NNM6 is overlooked as the underlying LNM was not considered in the ROB. The second ROM, $\mathbf{\Psi}_2^2$, is built using $[\boldsymbol{\phi}_2\ \boldsymbol{\phi}_6\ \boldsymbol{\theta}_{22}\ \boldsymbol{\theta}_{26}\ \boldsymbol{\theta}_{66}]$. Similarly to $\mathbf{\Psi}_1^2$, the overall NNM is well captured and the interaction with the mode that is outside the ROB is ignored. Furthermore, the secondary tongues are also neglected. Finally, a ROM, $\mathbf{\Psi}_3^2$, including the three LNMs and their corresponding MDs allows to accurately capture the NNM, including both primary interactions. This example shows that reduction basis made of LNMs and MDs can be built in a very systematic manner, based on the selection of the NNMs and modal interactions of interest. The latter can be identified based on the ratios between LNM natural frequencies and their proximity to a integer value.

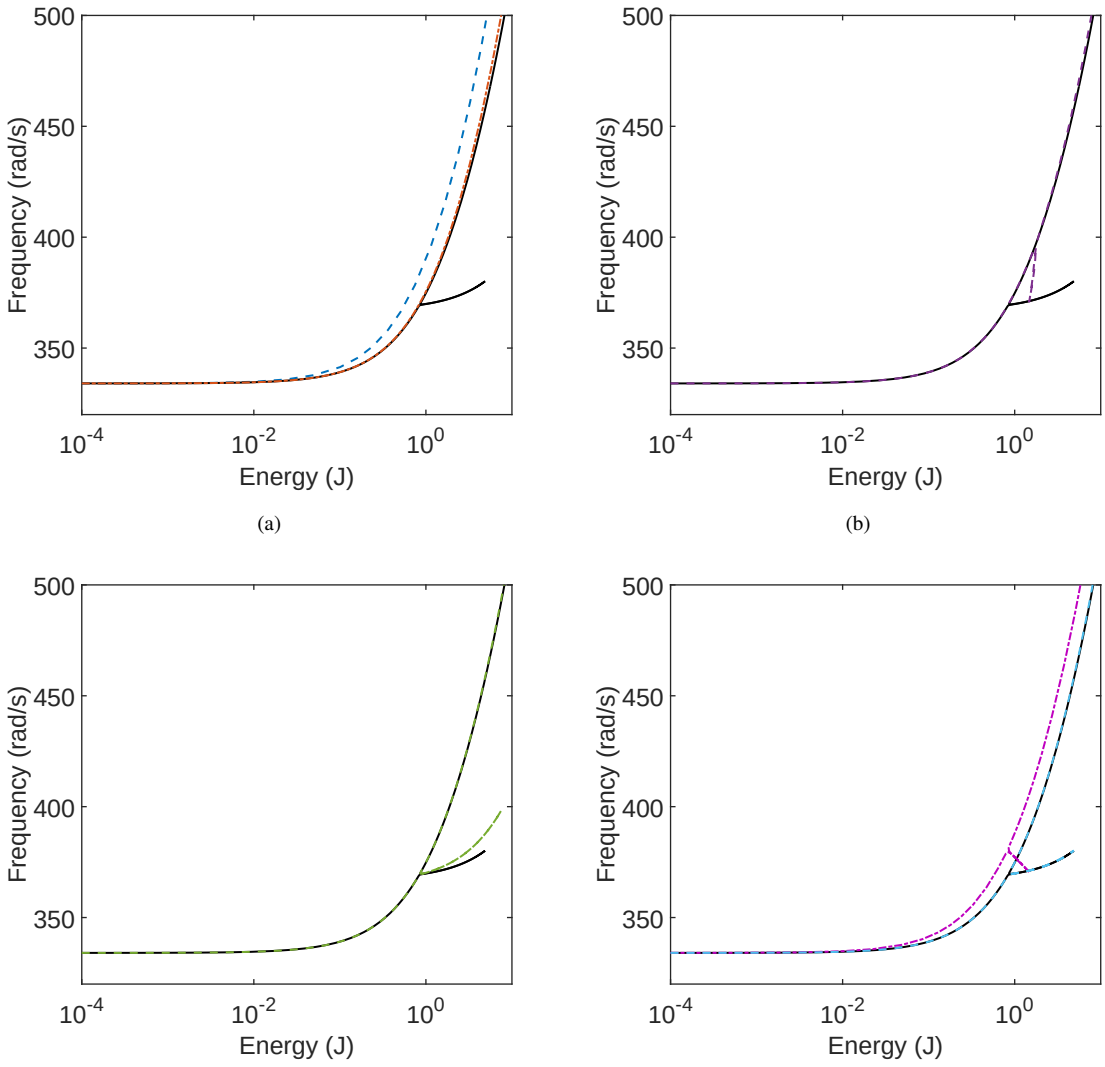

Figure 8: Comparison between NNM1 computed using the full model (—) and different ROMs: (a) $\mathbf{\Psi}_1 = [\boldsymbol{\phi}_1]$ (— —) and $\mathbf{\Psi}_2 = [\boldsymbol{\phi}_1\ \boldsymbol{\theta}_{11}]$ (— • —); (b) $\mathbf{\Psi}_3 = [\boldsymbol{\phi}_1\ \boldsymbol{\phi}_3\ \boldsymbol{\theta}_{11}]$ (— —); (c) $\mathbf{\Psi}_4 = [\boldsymbol{\phi}_1\ \boldsymbol{\phi}_3\ \boldsymbol{\theta}_{11}\ \boldsymbol{\theta}_{13}]$ (— —); (d) $\mathbf{\Psi}_5 = [\boldsymbol{\phi}_1\ \boldsymbol{\phi}_3\ \boldsymbol{\theta}_{11}\ \boldsymbol{\theta}_{13}\ \boldsymbol{\theta}_{33}]$ (— —) and $\mathbf{\Psi}_5 = [\boldsymbol{\phi}_1\ \ldots\ \boldsymbol{\phi}_5]$ (— • —).

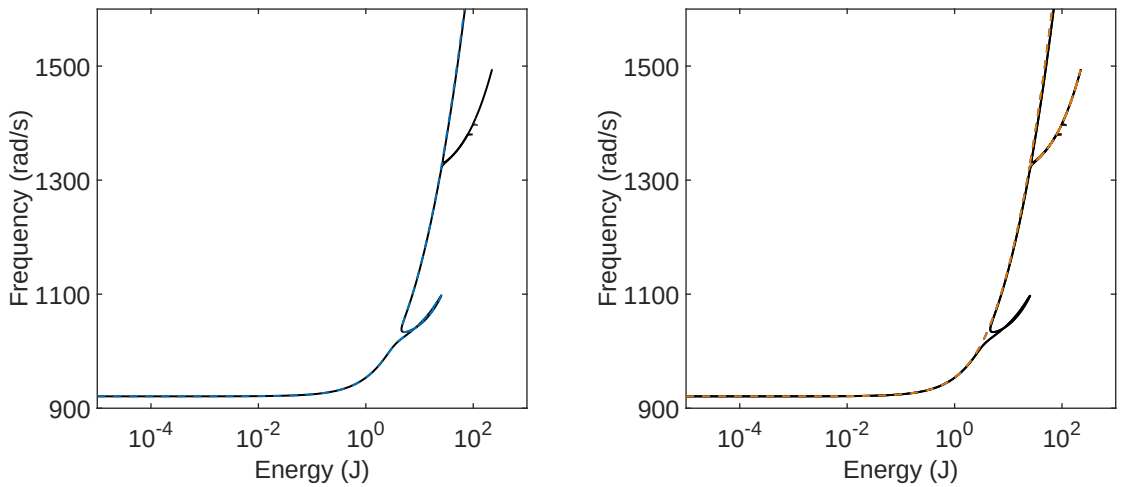

(a)

(b)

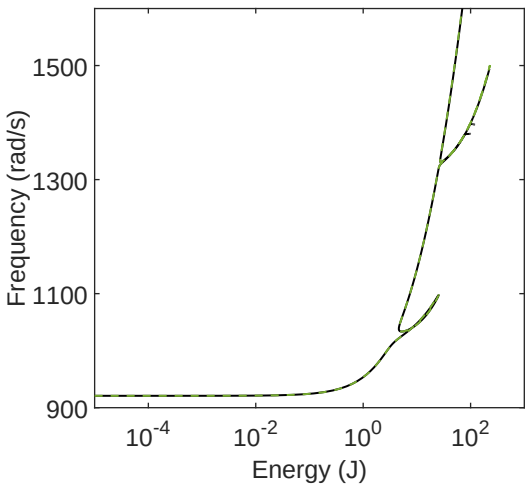

(c)

Figure 9: Comparison between NNM2 computed using the full model (▬) and different ROMs: (a) $\mathbf{\Psi}_1^2 = [\boldsymbol{\phi}_2\ \boldsymbol{\phi}_4\ \boldsymbol{\theta}_{22}\ \boldsymbol{\theta}_{24}\ \boldsymbol{\theta}_{44}]$ (▬ ▬); (b) $\mathbf{\Psi}_2^2 = [\boldsymbol{\phi}_2\ \boldsymbol{\phi}_6\ \boldsymbol{\theta}_{22}\ \boldsymbol{\theta}_{26}\ \boldsymbol{\theta}_{66}]$ (▬ ▬); (c) $\mathbf{\Psi}_3^2 = [\boldsymbol{\phi}_2\ \boldsymbol{\phi}_4\ \boldsymbol{\phi}_6\ \boldsymbol{\theta}_{22}\ \boldsymbol{\theta}_{24}\ \boldsymbol{\theta}_{44}\ \boldsymbol{\theta}_{26}\ \boldsymbol{\theta}_{46}\ \boldsymbol{\theta}_{66}]$ (▬ ▬).

4.3. Example 3: Arch

In this final example, a shallow arch obtained by curving the beam presented in Section 4.2 is considered. The curvature is such that the middle of the beam is displaced vertically by 1cm, which corresponds to 1% of the beam length. The mechanical properties of the beam are the same as in Section 4.2; its geometry is shown in Figure 10. The first three LNMs of this shallow arch are similar to those of the straight beam, except that they now include non-zero lateral displacements (along the x axis). However, as a result of the relatively small curvature applied, lateral displacements remain at least one order of magnitude smaller than vertical displacements for all three modes. The first LNM also shows a significantly higher natural frequency ($\approx$40%) due to the curvature effects.

The MDs of the first three LNMs are presented in Figure 11. The beam curvature and the presence of both lateral and vertical displacements in the LNMs lead to MDs with both lateral ($--$) and vertical ($-\,-$) components. As show in Figure 11, the form of the lateral component is qualitatively similar to the case of the straight beam (see Figure 6) and appears to be, in general, smaller than the vertical component.

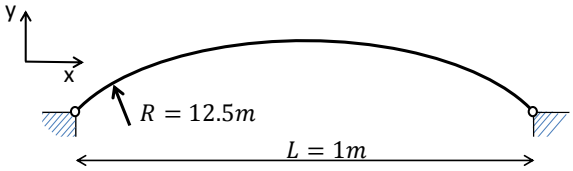

Figure 10: Sketch of the shallow-arch structure.

4.3.1. First NNM

The first NNM of the shallow-arch structure is presented in Figure 12. The FEP exhibits first a softening behaviour where the oscillation frequency decreases as energy increases, and then a hardening behaviour where the oscillation frequency increases. This softening-hardening behaviour is typical of curved and pre-stressed structures with geometric nonlinearities, as already reported in the literature. In the softening region, a 4:1 internal resonance between NNM1 and NNM3 is observed. Compared to the straight-beam structure that has a 5:1 interaction between the same modes, the interaction ratio is lower due the higher frequency of LNM1 caused by the initial curvature. The asymmetry introduced by curvature also increases the importance of the quadratic terms present in the geometric nonlinearity, which facilitates the appearance of interactions of even order. Interestingly, at the tip of the interaction tongue, the response of the structure is dominated by LNM3 but contains a static contribution from LNM1. This is illustrated by the modal configuration plot inset in Figure 12 where the motion of the structure has been decomposed into the first, η_1, and third, η_3, linear modal coordinates. η_1 remains negative during the entire periodic motion, suggesting a sort of 'static compression' of the arch. The deformation of the structure ($-$) at four periodic solutions along the FEP is also compared to the underformed structure ($-\,-$) in Figures 12(a-d). Along the main NNM branch, the structure is predominantly deformed according to its first LNM. Along the modal interaction tongue, the structure deformation results from a combination of LNM1 and LNM3 as already illustrated by the modal configuration plot inset the FEP. After the interaction tongue, the contribution of LNM3 first decreases and then increases again as illustrated by the deformation of the structure at point (d). However, at this point, displacements exceed the beam thickness and the model is no longer valid. We note that displacements at points (a-c) remain below 1mm, the thickness of the beam.

Figure 12 also includes the FEP obtained with three different ROMs. As previously observed in the straight-beam example, the ROM built using the first LNM, $\boldsymbol{\phi}_1$, does not capture well the NNM. Although the obtained FEP shows a softening-hardening behaviour, the frequency-energy dependence of the NNM is quantitatively wrong as soon as nonlinear distortions become visible, i.e. above 10^{-2} J. The addition of $\boldsymbol{\theta}_{11}$ to the ROB provides a significant improvement, allowing to represent the softening region for changes in frequency of approximately 7%, which corresponds to a displacement amplitude of 55% of the cross section thickness at the midspan point. Yet, this model is not able to capture the internal resonance behaviour and the frequency where the transition to hardening occurs is overestimated by approximately 15 rad/s, i.e. 3% of the natural frequency. Finally, the ROM containing

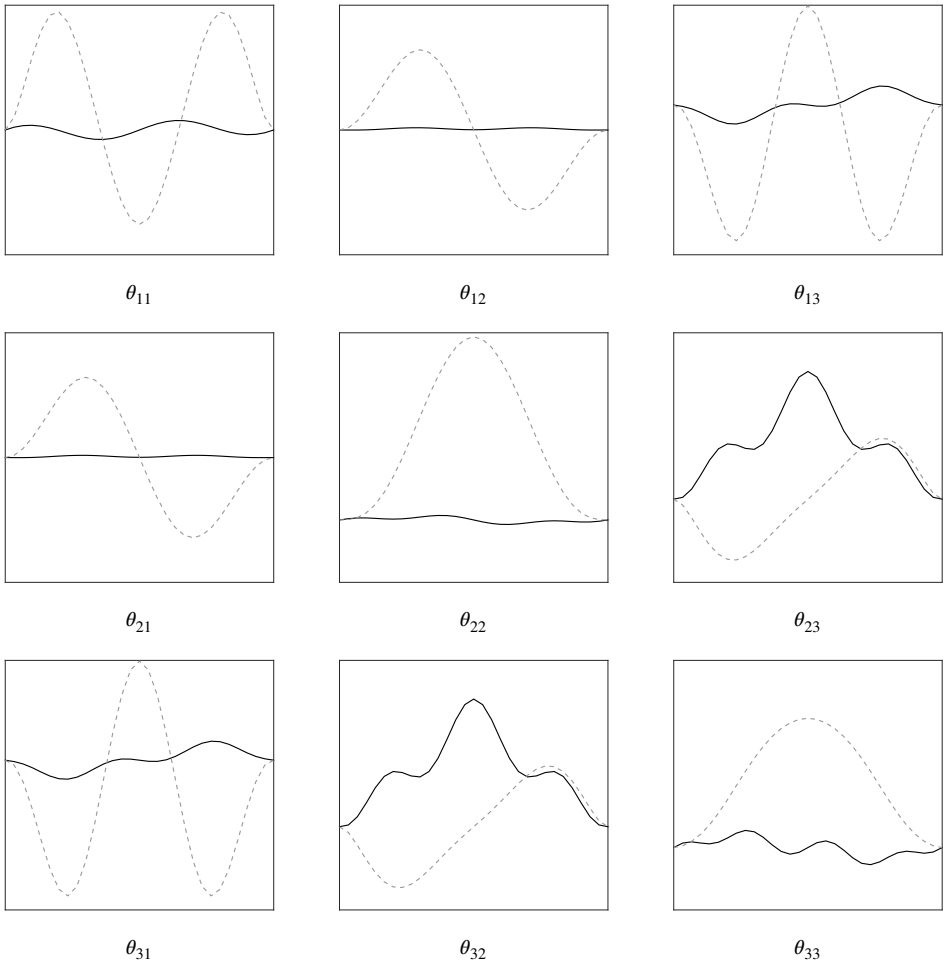

Figure 11: MDs of the first three LNMs with respect to each other for the shallow arch system. MDs exhibit components in both lateral (▬) and vertical (▬) direction (both represented on the vertical axis for clarity).

five DOFs, the two LNMs and their 3 MDs, is able to accurately follow the softening behaviour, capture the internal resonance, and predict the hardening effect with small errors both in frequency and energy.

4.3.2. Second NNM

The FEP of the second NNM shows the presence of a very complex nonlinear dynamic behaviour not encountered in the previous examples (see solid black line in Figure 13). The FEP exhibits a 3:1 interaction between NNM2 and NNM4. Contrary to the straight-beam example where interactions were located in a narrow frequency region, the interaction observed in Figure 13 exists for a wide range of frequencies and energies. Many secondary branches corresponding to high-order interactions between sometimes more than two LNMs emanate from the main 3:1 tongue. Figure 13 shows the response of the structure projected onto the basis of LNMs for a point located on one of the secondary branches (highlighted by a diamond marker in Figure 13). As this branch comes from the interaction between NNM2 and NNM4, both LNM2 and LNM4 contribute significantly to the response of the system. The response also includes components from LNMs 10-12 and static contributions from LNM1 and LNM3.

The reproduction of the second NNM using different ROMs is also reported in Figure 13. Contrary to the previous examples and the first NNM of this shallow arch system, a 2DOF ROM containing $\boldsymbol{\phi}_2$ and $\boldsymbol{\theta}_{22}$ does not capture well the overall shape of the NNM (−−). This can be explained, at least partially, by the presence of the static contributions introduced by LNM1 and LNM3 which are not accounted for in the ROB. Furthermore, the internal resonance is not reproduced as LNM4 is not included in the ROB. A good representation of the FEP (−−), including

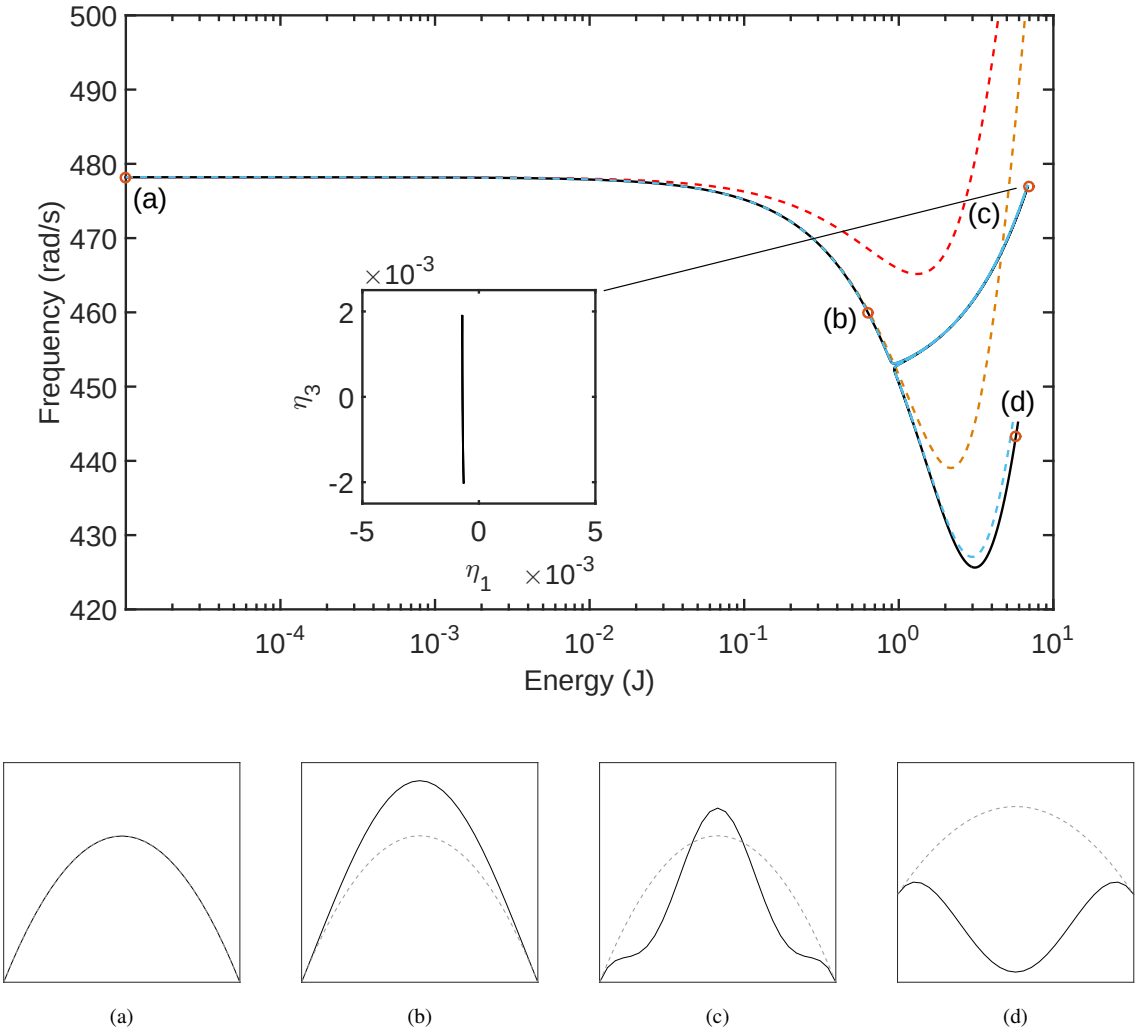

Figure 12: First NNM of the shallow arch structure. FEP computed for the full model (—), a ROM containing $\boldsymbol{\phi}_1$ (— —), a ROM containing $[\boldsymbol{\phi}_1\ \boldsymbol{\theta}_{11}]$ (— —), and a ROM including $[\boldsymbol{\phi}_1\ \boldsymbol{\phi}_3\boldsymbol{\theta}_{11}\ \boldsymbol{\theta}_{13}\boldsymbol{\theta}_{33}]$ (— —). Modal configuration plot representing the time evolution of the third linear modal coordinate, η_3, as a function of the first one, η_1, is inset for the periodic solution at the tip of the 4:1 modal interaction tongue. (a-d) Comparison between deformed (—) and undeformed (— —) structures for four periodic responses highlighted in the FEP (○).

the 3:1 interaction but excuding the secondary branches, is obtained for a ROM with the first four LNMs and their corresponding MDs (for a total of 14 DOFs). A small error in the prediction of the tip of the main interaction tongue can however be observed (see Figure 13(b)).

Interestingly, this last ROM revealed useful for computing the FEP of the full system. Indeed, as already pointed out in the straight beam example, the numerical continuation algorithm experienced a very slow progress while computing secondary (high-order) interaction branches. To overcome this issue, the continuation algorithm was restarted at different points along the main 3:1 interaction using the solution obtain from the ROM as initial guess for the solution of the full system. In this way, the full computation of the secondary branches was unnecessary to progress along the main interaction. As a result, the FEP obtained for the full system is made of 14 continuation runs, all of which were started thanks to the ROM. Note also that the continuation step was imposed to be large in order to skip as many secondary branches as possible.

The reproduction of the secondary interactions using richer ROBs was attempted. The results obtained with ROMs containing 27 DOFs (— —) and 35 DOFs (— —) are plotted in Figure 13(b) where a close-up of the main interaction

	Total time (seconds)	Newmark implicit (seconds)	$\mathbf{f}^{\text{nl}}$ (seconds)	$\mathbf{K}^{\text{nl}}$ (seconds)
Full model (87 DOFs)	9	1.4 (15%)	3.3 (37%)	4.3 (48%)
Ψ_5 (5 DOFs) full-model nonlinearities.	6.8	0.2 (3%)	2.8 (41%)	3.9 (57%)
Ψ_5 (5 DOFs) Tensor nonlinearities	0.55	0.18 (33%)	0.18 (33%)	0.19 (34%)

Table 3: Computational time required to perform the time integration of one periodic solution in the case of the shallow arch example. Total integration time is the sum of the evaluation time of Newmark's formulae, nonlinearities $\mathbf{f}_{\text{nl}}$ and their derivatives $\mathbf{K}_{\text{nl}}$. 500 time steps were considered. Percentages in brackets represent the relative importance of the computational time (columns 2-4) compared to the total time (first column).

is given. The ROM totalling 27 (resp. 35) DOFs includes the first five (resp. seven) LNMs and the corresponding MDs.

The structure of the interactions obtained when using 27 DOFs is very complex. The path followed by the FEP is organised according to the numbers provided in Figure 13(b). Starting from low energies (at the bottom-left corner of the figure), a first interaction which was not present in the previous ROMs, is observed around 1045 rad/s (point (1)). Although present in the FEP of the full system, this interaction starts at a lower energy. The path from (1) to (3) is not observed in the full solution. Moving from (3) to (4), the FEP follows a path present in the full system, yet at a lower frequency. From (4), the FEP goes back to the main resonance tongue and goes up to point (5). Eventually, the FEP goes back down again and ends in (6), where the continuation algorithm could no longer progress. Note that this ROM slightly improves the FEP in the region of the main interaction compared to the 14-DOF ROM.

The 35-DOF ROM captures accurately the beginning of the first secondary branch observed on the FEP of the full system. However, halfway along this branch the FEP starts to deviate from the full solution and, eventually, the continuation algorithm could not progress any further.

5. A Note on the Computational Cost

The combined use of LNMs and MDs provides an accurate ROB for geometrically nonlinear systems. However, the use of such ROBs alone provides only marginal improvements in terms of computational costs. In particular, the cost of time integration represents, for the examples considered, up to 95% of the total cost of the NNM calculation. Table 3 presents the cost of the time integration of one periodic solution for the first NNM of the shallow arch example. For the full model, 85% of the time lies in the evaluation of the nonlinear force vector $\mathbf{f}^{\text{nl}}$ and the tangential stiffness matrix $\mathbf{K}^{\text{nl}}$ (required by the implicit time integration scheme adopted here and the shooting algorithm). When considering the ROM Ψ_5 (see Section 4.3.1), the number of degrees of freedom drops from 87 to 5. As a consequence, the time required to evaluate implicit time integration formulae decreases from 1.4 seconds to 0.2 seconds. It is expected that greater relative reductions would be achieved in real-life industrial applications, as they usually feature larger dimensionality than the three examples considered here. It can be noticed, however, that the overall cost of the time integration does not reflect the same reduction observed with Newmark's formulae because the evaluation of the nonlinearities still requires function calls and assembly over the entire mesh, which scales with the size of the full model. Similar trends were noticed on the Roorda's frame and straight beam examples.

To further reduce computational cost, one has to address more efficiently the computation of the nonlinear terms and their derivatives. An approach is to use the so-called hyper reduction techniques as, for instance, the DEIM method [28], its variant proposed in Ref. [29], and the more recent ECSW method [30]. These methods selectively pick a short number of elements to compute the reduced nonlinear force vector and its derivatives. An alternative which would still consider an exact representation of the nonlinear terms is to rewrite the nonlinearities in tensorial forms directly in *modal* coordinates. For the adopted von-Karman kinematics, this will result in quadratic and cubic nonlinear terms. The third- and fourth-order tensors of constant coefficients can be computed offline, in a similar way to the reduced linear mass and stiffness matrices, $\hat{\mathbf{M}}$ and $\hat{\mathbf{K}}$, in Eq. (4), see for instance [18]. In this latter case, the equations of motion are reduced to a form similar to the one used in other nonlinear model reduction techniques

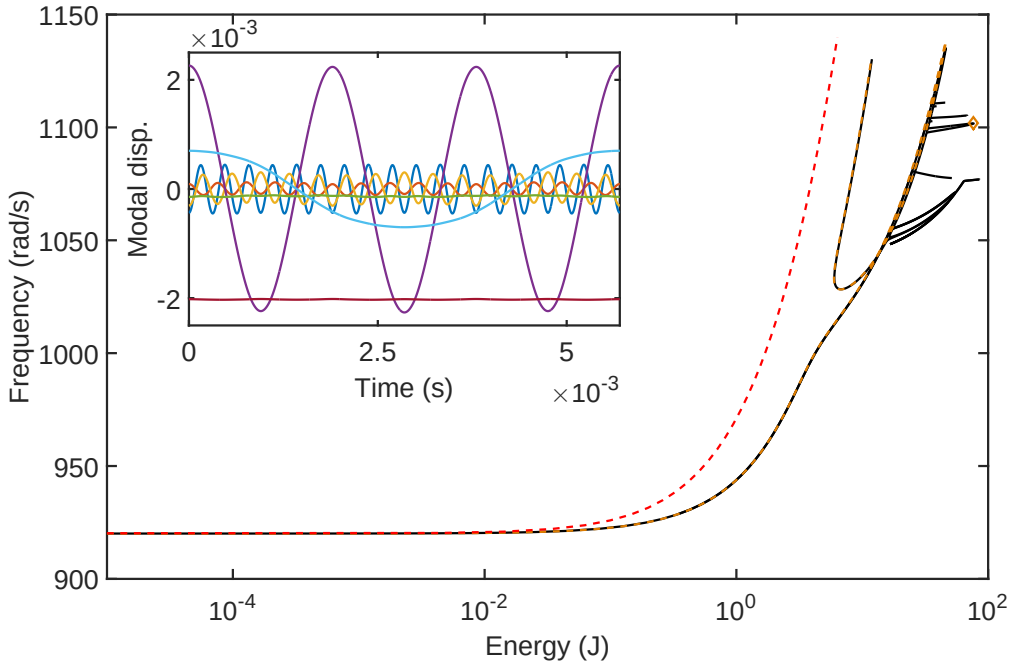

(a)

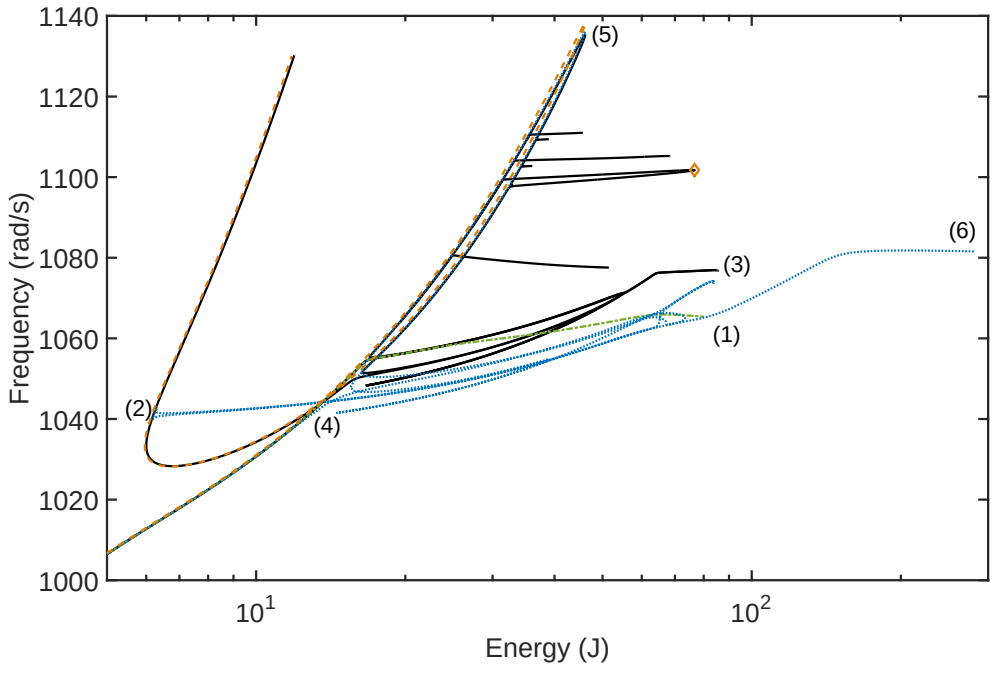

(b)

Figure 13: Second NNM of the shallow arch structure. FEP computed for the full model (—), a ROM containing [$\boldsymbol{\phi}_2$ $\boldsymbol{\theta}_{22}$] (— —), a ROM containing [$\boldsymbol{\phi}_2$ $\boldsymbol{\phi}_4\boldsymbol{\theta}_{22}$ $\boldsymbol{\theta}_{24}\boldsymbol{\theta}_{44}$] (— —), and ROMs including the first five (resp. seven) LNMs and the corresponding MDs ((— —)) (resp. ((— —))). Modal time series for periodic solution ◇ are inset Figure 13(a): η_1 (—), η_2 (—), η_3 (—), η_4 (—), η_{10} (—), η_{11} (—), η_{12} (—).

as, for instance, the ICE method [11], and similar calculation speed-ups can be expected. Table 3 shows that the tensor approach leaves the evaluation time of Newmark's formulae almost unchanged but significantly reduces the time required to compute $\mathbf{f}^{\text{nl}}$ and $\mathbf{K}^{\text{nl}}$. As such, the overall computational time is reduced by a factor of $\approx$16 compared to the original full model.

Besides the actual cost of time integration, the use of ROMs presents another significant advantage. ROMs were found to considerably reduce the complexity of the nonlinear dynamics, removing, for instance, secondary interaction tongues between higher-frequency modes. The relevance of interactions between such modes is questionable, even for the full system, as they are, in general, very sensitive to the finite element (spatial) discretization. The convergence of the continuation algorithm was also observed to be better compared to the full model. Overall this led to a faster computation of all the FEPs.

6. Conclusions

The computation of nonlinear normal modes of autonomous and conservative geometrically nonlinear systems can be very time consuming, even for low-dimensional structures as the one considered here. To address this issue, this paper proposed to use reduced-order models obtained by Galerkin projection on a reduction basis composed of vibration modes and the corresponding modal derivatives. Such reduced-order models were shown to accurately capture the overall trend of the frequency-energy plot. Numerical examples also showed that all the modal derivatives associated with two - or more - interacting modes are a priori necessary to accurately reproduce internal resonance tongues that occur when linear modes interact via nonlinear coupling at commensurate frequencies. Reproducing these results using reduced order models comprising linear vibration modes only was also shown to require larger reduction basis. The crisp physical interpretation of modal derivatives combined with their clear role in capturing the dynamic features of the nonlinear system lead to a systematic construction of the reduced-order model without a priori knowledge of the nonlinear normal mode of the full system.

Significant computational gains were obtained when combining the reduced-order model with a modal tensorial form of the nonlinear forces. Alternatively, the use of hyper-reduction is advocated. Another benefit of resorting to reduced order models for the computation of nonlinear normal modes is the natural filter that modal truncation provides. As such, the 'spurious dynamics', i.e. high-order interaction tongues associated with high-frequency linear modes, that caused computational difficulties on the full model is excluded from the reduced-order model. Contrary to linear modes, the introduction of modal derivatives in the reduction basis in order to capture nonlinear bending-stretching effects does not appear, for the examples considered, to reintroduce this 'spurious dynamics'.

The addition of material nonlinearities *of conservative type* does not pose any fundamental difficulty to the applicability of this reduction method. For dissipative nonlinearities, as for instance friction or plasticity, one should resort to the definition of a NNM as an invariant manifold.

Acknowledgements

The project leading to this application has received funding from the European Union's Horizon 2020 research and innovation programme under the Marie Sklodowska-Curie grant agreement No 703204. L.R. was also partly funded by the Royal Academy of Engineering (research fellowship RF1516/15/11).

References

[1] H. H. Mian, G. Wang, Z.-Y. Ye, Numerical investigation of structural geometric nonlinearity effect in high-aspect-ratio wing using cfd/csd coupled approach, Journal of Fluids and Structures 49 (0) (2014) 186–201.

[2] L. Renson, J. P. Noël, G. Kerschen, Complex dynamics of a nonlinear aerospace structure: numerical continuation and normal modes, Nonlinear Dynamics 79 (2) (2015) 1293–1309.

[3] B. Strachan, S. Shaw, O. Kogan, Subharmonic resonance cascades in a class of coupled resonators, Journal of Computational and Nonlinear Dynamics 8 (4) (2013) 041015.

[4] N. Boechler, G. Theocharis, C. Daraio, Bifurcation-based acoustic switching and rectification, Nat Mater 10 (9) (2011) 665–668.

[5] R. M. Rosenberg, Normal modes of nonlinear dual-mode systems, Journal of Applied Mechanics 27 (2) (1960) 263–268.

[6] Y. S. Lee, G. Kerschen, A. F. Vakakis, P. Panagopoulos, L. Bergman, D. M. McFarland, Complicated dynamics of a linear oscillator with a light, essentially nonlinear attachment, Physica D: Nonlinear Phenomena 204 (1-2) (2005) 41–69.

[7] L. Renson, G. Kerschen, B. Cochelin, Numerical computation of nonlinear normal modes in mechanical engineering, Journal of Sound and Vibration 364 (2016) 177–206.

[8] G. Kerschen, M. Peeters, J. C. Golinval, C. Stéphan, Nonlinear modal analysis of a full-scale aircraft, Journal of Aircraft 50 (5) (2013) 1409–1419.

[9] R. Craig, Coupling of substructures for dynamic analysis, AIAA journal 6 (1968) 1313–1319.

[10] S. Rubin, Improved component-mode representation for structural dynamic analysis, AIAA journal 13 (8).

[11] J. J. Hollkamp, R. W. Gordon, Reduced-order models for nonlinear response prediction: Implicit condensation and expansion, Journal of Sound and Vibration 318 (4-5) (2008) 1139–1153.

[12] R. Kuether, B. Deaner, J. Hollkamp, M. Allen, Evaluation of geometrically nonlinear reduced-order models with nonlinear normal modes, AIAA Journal 53 (11) (2015) 3273–3285.

[13] S. Idelsohn, A. Cardona, A reduction method for nonlinear structural dynamic analysis, Computer Methods in Applied Mechanics and Engineering 49 (3) (1985) 253–279.

[14] P. Tiso, Optimal second order reduction basis selection for nonlinear transient analysis, in: Modal Analysis Topics, Volume 3, Springer, 2011, pp. 27–39.

[15] P. Tiso, D. J. Rixen, Reduction methods for MEMS nonlinear dynamic analysis, Springer New York, New York, NY, 2011, pp. 53–65. doi:10.1007/978-1-4419-9719-7_6.
URL http://dx.doi.org/10.1007/978-1-4419-9719-7_6

[16] F. Wenneker, P. Tiso, Proceedings of the 32nd imac, a conference and exposition on structural dynamics, in: Springer (Ed.), Dynamics of Coupled Structures, Vol. 1, 2014.

[17] O. Weeger, U. Wever, B. Simeon, Nonlinear frequency response analysis of structural vibrations, Comput. Mech. 54 (6) (2014) 1477–1495.

[18] L. Wu, P. Tiso, Nonlinear model order reduction for flexible multibody dynamics: a modal derivatives approach, Multibody System Dynamics (2015) 1–21.

[19] M. Crisfield, Non-linear Finite Element Analysis of Solids and Structures, John Wiley and Sons. Inc., 1991.

[20] R. Nickell, Nonlinear dynamics by mode superposition, Computer Methods in Applied Mechanics and Engineering 7 (1) (1976) 107–129.

[21] N. F. Morris, The use of modal superposition in nonlinear dynamics, Computers & Structures 7 (1) (1977) 65–72.

[22] S. Remseth, Nonlinear static and dynamic analysis of framed structures, Computers & Structures 10 (6) (1979) 879–897.

[23] S. R. Idelsohn, A. Cardona, A load-dependent basis for reduced nonlinear structural dynamics, Computers & Structures 20 (1-3) (1985) 203–210.

[24] R. B. Nelson, Simplified calculation of eigenvector derivatives, AIAA Journal 14 (9) (1976) 1201–1205.

[25] M. Géradin, D. Rixen, Mechanical vibrations: theory and application to structural dynamics, John Wiley, 1997.

[26] M. Peeters, R. Viguié, G. Sérandour, G. Kerschen, J. C. Golinval, Nonlinear normal modes, part II: Toward a practical computation using numerical continuation techniques, Mechanical Systems and Signal Processing 23 (1) (2009) 195–216.

[27] P. Tiso, Finite element based reduction methods for static and dynamic analysis of thin-walled structures, Ph.D. thesis, Delft University of Technology (2006).

[28] S. Chaturantabut, D. Sorensen, Nonlinear model reduction via discrete empirical interpolation, SIAM J. Sci. Comput. 32 (5) (2010) 2737–2764.

[29] P. Tiso, R. Dedden, D. Rixen, A modified discrete empirical interpolation method for reducing non-linear structural finite element models, in: 9th International Conference on Multibody Systems, Nonlinear Dynamics, and Control Portland, Oregon, USA, Vol. 7B, 2013.

[30] C. Farhat, T. Chapman, P. Avery, Structure-preserving, stability, and accuracy properties of the energy-conserving sampling and weighting method for the hyper reduction of nonlinear finite element dynamic models, International Journal for Numerical Methods in Engineering 102 (5) (2015) 1077–1110.